

Morphological Filter Detector for Forensics Applications

Giulia Boato

University of Trento, Italy

Duc-Tien Dang-Nguyen

University of Bergen, Norway

Francesco G. B. De Natale

University of Trento, Italy

Abstract

Mathematical morphology provides a large set of powerful non-linear image operators, widely used for feature extraction, noise removal or image enhancement. Although morphological filters might be used to remove artifacts produced by image manipulations, both on binary and graylevel documents, little effort has been spent towards their forensic identification. In a previous work [1], a deterministic approach was proposed to detect erosion and dilation of binary images. In this paper we propose a non-trivial extension of such method that operates on grayscale images and is robust to image compression and other typical attacks. When the image is attacked the method loses its deterministic nature and uses a properly trained SVM classifier, using the original detector as a feature extractor. Extensive tests demonstrate that the proposed approach guarantees very high accuracy in filtering detection also after a high compression, and is also able to determine the adopted structuring element for moderate compression factors.

Keywords: Morphological Filter Detection, Image Forensics

*Corresponding author

Email address: `boato@disi.unitn.it` (Giulia Boato)

1. Introduction

In the last decade, researchers and practitioners in multimedia forensics have been developing a substantial body of knowledge and techniques targeted to the authentication of multimedia objects and their processing history recovery [2, 3, 4, 5, 6]. A recent trend tries to define universal detectors able to reveal manipulations independently from the type of processing applied, which could leverage media authentication in applications like journalism or social media analysis [7]. On the other hand, many methods have been proposed to detect different types of forgeries, which is very relevant for diverse applications, in particular digital investigations - given that images, audio tracks and video sequences now play a crucial role in modern investigations where they often represent digital evidences to the court [8] - and multimedia data phylogeny aiming at recovering and tracing back the life-cycle of an image or a video [9, 10, 11, 12].

This broad class of specific manipulation detectors includes the identification of pasted or inserted regions [13, 14, 15, 16, 17], resizing [18], re-compression [19], inconsistencies in the geometry and illumination of the image due to possible manipulations [20, 21, 22], and various types of non-linear filtering (especially median) [23, 24, 25, 26, 27, 28, 29, 30, 31, 32].

In the context of non-linear filtering detection very little attention was given to morphological filters [33] often used in image processing for artifacts removal and image enhancement [34] [35]. The detection of this kind of filtering is of interest in the context of both image phylogeny and specific tampering identification in legal scenarios, but could be very useful also to detect possible counter forensic attacks based on morphology, where such filters, very powerful in the removal of local noise, could be exploited at the end of the image manipulation process to cover other types of traces.

In this paper we present a non trivial extension of a recent work [1] which deterministically detect erosion and dilation of binary images. The proposed extension works on grayscale images by detecting morphological filters application

in an accurate way both in uncompressed and compressed images. The method also allows for erosion versus dilation discrimination and in many cases also for the adopted structural element identification. Robustness against JPEG compression, noise addition and confusion with other types of filters is also tested
35 on various datasets.

The rest of the paper is organized as follows: Section II provides the theoretical background for the problem formulation; Section III describes the proposed methodology for morphological filtering detection in uncompressed and compressed images; Section IV describes the experimental setup, datasets and
40 scenarios adopted for testing and validation; Section V details the experimental analysis and obtained results; finally, Section VI reports some concluding remarks.

2. Theoretical formulation

In this section we introduce the mathematical formulation of the problem,
45 and we derive the proposed methodology for morphological filter detection.

2.1. Mathematical Formulation and Properties

Mathematical morphology defines a set of nonlinear filters commonly employed in digital image processing to modify the local structural content of images. All the morphological filters are derived from the various combinations
50 of two basic operators, *erosion* and *dilation*, and a kernel mask called *structuring element*, characterized by a shape, a size, and a reference point. The shape and the size of the kernel are responsible for the behavior of the operator on the image, while the reference point just defines the shift of the filtered image with respect to the original. The invention of such mathematical tools dates back to
55 1964 [33], and was meant to the filtering of binary images for mineral studies. Later studies [36] led to the generalization of the theory to the case of grayscale images.

According to this theory, given a grayscale image $f(x, y)$ and a binary structuring element B , the two fundamental morphological operators, erosion and dilation, are respectively defined as:

$$f \ominus B = \min_B(f(x, y) \cap B_{xy}) \quad (1)$$

$$f \oplus B = \max_B(f(x, y) \cap B_{xy}) \quad (2)$$

where B_{xy} represents the structuring element B with the reference point centered at the coordinates x, y of the image plane, while the intersection operations returns the subset of the image pixels overlapped with the 1s of B . In this respect, the basic grayscale operators are particular cases of rank-order filters, and behave very similarly to min-max and median operators, except for the shape of the mask.

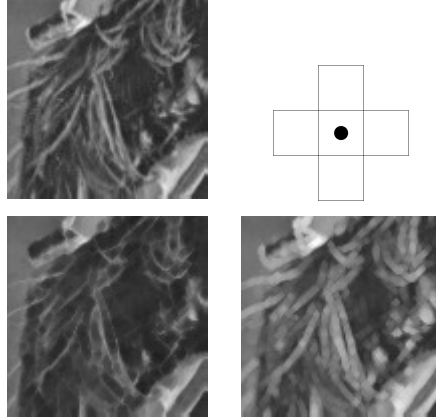


Figure 1: Example of gray-scale erosion (bottom left) and dilation (bottom right) of an image detail (top left), using a cross-shaped structuring element (top right). The resulting patches show the effect of min and max operations: erosion produces a darker version of the original image eliminating small cross-shaped details, while dilation produces the opposite effect.

As in binary morphology, the composition of erosion and dilation allows defining more complex filters, among which the most common are the *open* and *close* operators, respectively defined as follows:

$$(f \circ B) = (f \ominus B) \oplus B \quad (3)$$

$$(f \bullet B) = (f \oplus B) \ominus B \quad (4)$$

Also the mathematical properties of morphological grayscale operators match the ones of the corresponding binary operators. Consequently, the theoretical background of [1] remains valid also for in the grayscale domain. In particular, the following properties are exploited in the construction of the proposed
75 detector:

- (i) Translation invariance: the position of the reference point only affects the translation of the filtered image
- (ii) Dilation commutativity: $A \oplus B = B \oplus A$
- 80 (iii) Associativity: a cascade of erosions (dilations) is equal to the erosion (dilation) with a mask generated by dilating each other the original masks

$$A \ominus B \ominus C = A \ominus (B \oplus C) \quad (5)$$

$$A \oplus B \oplus C = A \oplus (B \oplus C) \quad (6)$$

- (iv) Open and close idempotence: iterating open and close with the same structural element does not produce additional changes in the image

$$A \circ B \circ B = A \circ B \quad (7)$$

$$A \bullet B \bullet B = A \bullet B \quad (8)$$

Additionally, it is easy to see that the two theorems introduced in [1] remain valid, since their demonstrations do not depend on Eq. 1 and Eq. 2, but only on the properties (i)-(iv), which hold also for greyscale images.

Theorem 1. *Let $C = A \ominus B$, then $C \bullet B = C$. Respectively, if $C = A \oplus B$,
90 then $C \circ B = C$.*

Theorem 2. *Let $C = A \ominus B$, then $\forall D$ such that $\exists E | D \oplus E = B$, we have that $C \bullet D = C$. Respectively, if $C = A \oplus B$, then $C \circ D = C$.*

Theorem 1 can be equivalently formulated in terms of series of erosion and dilation operators, according to the definition of open and close operators. Theorem 2 extends the equality of Theorem 1 to any mask D that can produce B by dilation with an appropriate mask E .

As an immediate consequence of the above theorems, an image dilated (eroded) with a given structural element B , will remain unchanged after applying an open (close) operator with the same element. This provides a simple test to detect a filtered image: apply an open (close) operator with a mask B , if the image does not change, this means that it was previously dilated (eroded) with that mask, otherwise it was not. The detection consists then in subsequently checking with the above procedure a set of possible masks. In [1], a set of common structural elements were proposed, characterized by some level of symmetry (see Figure 2).

3. Proposed approach

In this section we introduce the proposed detector, distinguishing two cases: the detection of morphological filtering on unattacked images, and the detection in the presence of attacks. We will see that the former is a trivial extension of the binary case but has very limited applicability, while the latter requires further attention.

3.1. Filter Detection on Unattacked Images

According to the theory stated in Section 2, in the absence of attacks grayscale morphological operators can be easily and deterministically detected by applying the schema proposed in [1] and reported in Figure 3.

However, it is worth mentioning that this scenario is rarely verified in grayscale images, which are typically stored in compressed format after filtering. The compression (as well as most other image processing operations) significantly

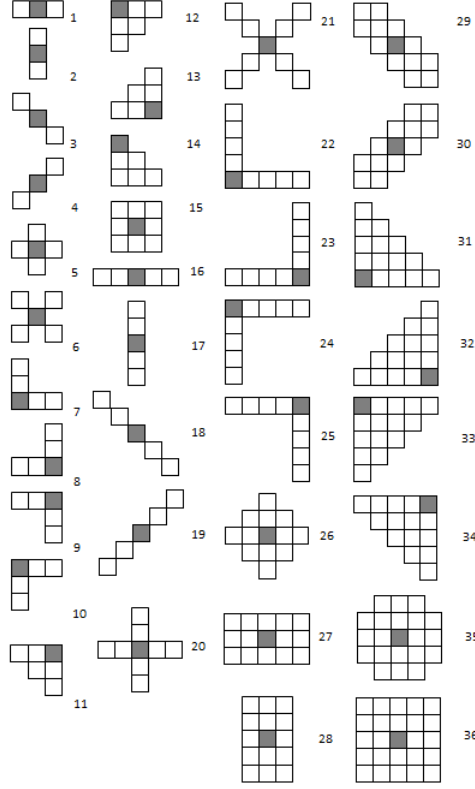


Figure 2: Set of kernels used for simulations. In grey, each structural element's reference point

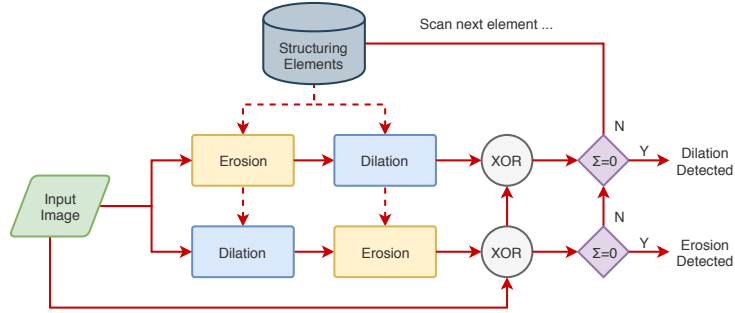


Figure 3: Proposed detection scheme for unattacked grayscale images

modifies the image, thus hindering the applicability of Theorem 1. As a result,
 120 the detector will never report a perfect match between the input eroded (di-
 lated) image and the corresponding opened (closed) version, i.e., it will never

output a positive detection.

In the next section we propose an extension of the above algorithm that is able to deal with such scenario. The new algorithm will exploit the traces left by the morphological filters even after post-processing, and will rely on a statistical analysis, thus losing its deterministic nature. We will see however that it is sufficiently robust to many attacks, and in particular to the JPEG compression.

3.2. Filter Detection on Attacked Images

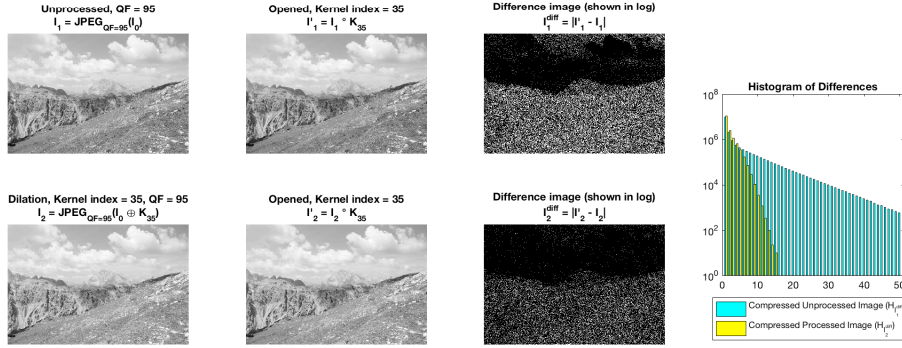


Figure 4: Histograms of differences before and after application of the open operator to an original image (gray scaled of 'r22fa37aft.TIF' from RAISE-1k) and its dilated version. Both images have been JPEG-compressed with $QF = 95$. The chart shows the first 50 bins in logarithmic scale. **I SUGGEST TO IMPROVE THE QUALITY OF THIS PICS, NOT VERY VISIBLE ON PRINTED DOCUMENT**

As mentioned in the previous section, any further processing of the filtered image will modify the pixel values, possibly re-introducing structures that were eliminated by the morphological operator. A further morphological filtering will then produce a non-null effect on the image, which will be revealed by the detector. It is therefore necessary to verify if some traces of the original filter survive the post-processing.

Recalling that the grayscale morphology operates as a local min-max filter, we can expect that it will produce larger variations in the presence of high-contrast structures that match the structural element geometry. On the

contrary, unless the post-processing is meant to be extremely visible, it will introduce small graylevel variations on the image. Consequently, although we will not have a null difference image at the detector output, we can expect that the local differences will be much smaller for a filtered image than for an original one. An experimental evidence of this fact is provided in Figure 4. Here we plot the log-scale histograms of the absolute differences before and after the application of an open operator to a JPEG-compressed unfiltered image, and to the relevant JPEG-compressed dilated image. Both open and dilation operators have been applied using the kernel mask 35 in Fig. 2, and the JPEG quality factor has been set to $QF = 95$. It is possible to observe that the histogram referred to the dilated image decreases steeply, with significant bins only for low values of the difference, while the histogram referred to the unfiltered image shows a long tail with significant values also above 50. This means on one side that the compression does not affect the high-contrast structures present in the original image (which are then removed by the following open operator), and on the other side that it does not re-introduce in the filtered image any high-contrast structure sensitive to the filter itself.

On this basis, we propose to modify the detection scheme as shown in Figure 5.

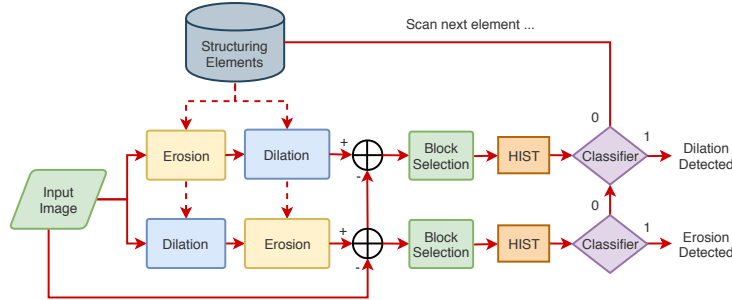


Figure 5: Proposed detection scheme for attacked grayscale images. **WHAT ABOUT USING A SINGLE BLOCK SELECTION AND SVM CLASSIFIER?**

The core of the procedure still involves the application of grayscale opening/closing. In this case, however, we take into consideration the statistical

properties of the differences between the input and output images, to see how
 160 such residual is distributed. Therefore, we calculate the histogram of the difference image and feed it into a statistical classifier to perform the decision. As far as the classifier is concerned, we adopted a properly trained SVM classifier. Details on the classifier are provided in the next section.

Finally, we should notice that not all the areas of an image are equally affected by a morphological filter. In particular, the filter has a negligible effect
 165 on flat areas, thus possibly jeopardizing the results of the detector. To avoid this problem we decided to limit the analysis to the image regions that contain significant textures or edges. To this purpose, we calculate the block-wise normalized local variance α , and we restrict the computation of the histogram to
 170 the blocks with $\alpha > \alpha_{th}$, where α_{th} has been empirically set to 0.15 (please see Sec. ?? for deeper discussion). This task is performed by the first processing block in Fig. 5.

4. Experimental setup

In order to assess the performance of the proposed detector, we tested it in
 175 various scenarios and we evaluated it in terms of accuracy. In this section we describe such scenarios and the relevant experiments. Furthermore, we introduce the datasets used for the testing, and we provide additional details about the SVM classifier used in the detector and the relevant training procedure.

4.1. Datasets

180 Three publicly available datasets have been used in the experiments:

- The Uncompressed Colour Image Database (UCID) [37], built with the purpose of providing a standard set for performance assessments in image retrieval and compression. The dataset consists of 1,338 uncompressed color images, with fixed sizes of 512×384 or 384×512 pixels in uncom-
 185 pressed TIFF format.

- The Dresden Image Database (DRESDEN) [38], originally created for evaluation of forensic techniques related to camera-based information. From their public web-interface, we selected the complete set of RAW images (1,189 uncompressed images, all with fixed size of 3008×2000 pixels).
- The Raw Images Dataset (RAISE) [39], consisting of 8156 raw images with resolutions ranging from 3008×2000 to 4928×3264 pixels. Authors provide also smaller subsets, among which we selected the one containing 1,000 images (RAISE-1k).

The three sets were selected to diversify the range of resolutions in the experimental tests. In order to evaluate our proposed schema, all the images were converted to grayscale with a depth of 8 bits.

4.2. Testing scenarios

The proposed detector has been tested in various practical scenarios. It is to be pointed out that we did not consider the case of unattacked images, which is by definition deterministic, as previously discussed, and provides therefore 100% accuracy.

The first set of tests refers to the detection of morphological filtering on compressed images, using JPEG at various quality factors. In this case, we want to establish the accuracy of the detector in discriminating filtered vs. unfiltered images, in classifying the type of operator (erosion vs. dilation), and finally in determining the exact structuring element used for filtering.

The second set of tests concerns noise attacks. In this case, the test image is contaminated with random noise and then compressed. Also in this case we determine the accuracy of the detector in determining the presence and type of filtering and the structuring element used.

Finally, we want to determine the capability of our approach in distinguishing between morphological filters and other filters that produce similar results. In particular, we considered Gaussian lowpass and median filtering. In both

215 cases, the filtered images are compressed and passed to the detector to reveal possible false alarms.

It is worth noting that, due to the properties analysed in Sect. 2, in the presence of a cascade of different basic operators (erosion and dilation), the detector will reveal the last operator applied. Accordingly, when processing an opened
220 or a closed image, the detector will reveal the last dilation or erosion, respectively. Furthermore, in the presence of a cascade of the same basic operator, the detector will reveal a single erosion or dilation with the composed structuring element. Therefore, in the experimental section we will just consider erosion and dilation detection, even if the image may have been potentially processed
225 with more complex combinations of filters.

4.3. The Sensibility and the Choice of the Classifiers

In order to understand the influence of the parameters as well as to select a proper classifier, we ran some experiments on a subset of images. After that, we empirically determined the values for these parameters. Table 1 summarizes
230 these parameters, their meaning and how their values were decided.

The classifier receives in input the histogram of the differences between the input image and the relevant opened (closed) image and returns a binary decision. An important aspect is the training of the classifier. In fact, there is a clear dependency of the image statistics on the level of compression applied,
235 which is reflected on the characteristics of the histogram. As an example, Fig. 6 shows the same situation of Fig. 4 at a lower quality factor. It can be observed that the two distributions are still well separable, but the histogram related to the filtered image shows a longer tail, due to the larger artifacts introduced by the compression.

240 Accordingly, we decided to train a set of classifiers for varying JPEG quality factors, from 100 to 70. During the test phase, the most appropriate classifier is selected on the basis of the QF retrieved by the image EXIF.

Given the appropriate quality factor, the histograms of differences show a peculiar behavior only if the detector parameters match the input filter in both

Table 1: Parameters selection.

Parameter/ Classifier	Meaning	Range	Empirical Value
Image resolution	The size of the analyzed region of interest	384×512 to 4928×3264	Good results for resolution higher than 1000×1000
Block Selection Threshold α_{th} and Block Size s	Erosion and dilation have a negligible effect on flat areas, thus these two parameters allow the method to effectively work on non-flat blocks only.	$\alpha_{th} \geq 0$, $\alpha = 0$ means all pixels in the block has the same values. $s \in \{3 \times 3, 5 \times 5, \dots\}$	$\alpha_{th} = 0.15$ and $s = 3 \times 3$
n	Number of bins of the analyzed histograms.	$0 \leq n \leq 256$	Even if for $n > 30$ we already achieve 90% accuracy, we choose n at the highest value, considering all bins.
The classifiers		SVM, KNN, Linear Regression, and others	SVM with RBF kernel and grid search provides the best performance, Sec. ??.

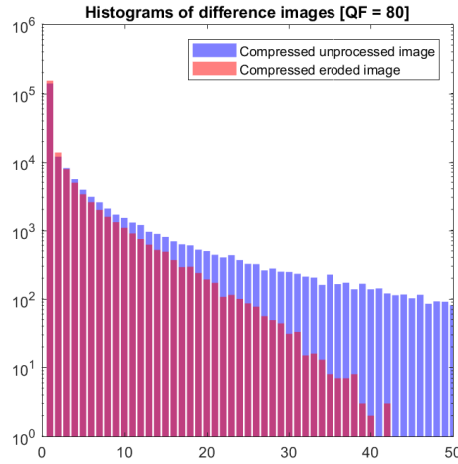


Figure 6: Same case of Fig. 4 after compression at $QF = 80$.

245 the operator (erosion or dilation) and the structural element, whereas such behavior is never found in all the other combinations. It is important to notice that the application of the detector to an unfiltered image or to an image filtered with a different combination of operator and/or structuring element produces similar results, i.e., only the matching detector responds to the filtered image.
 250 As an example, in Fig. 7 we show the histograms deriving from the application of an erosion detector to an eroded and a dilated image, both with the same structuring element. It can be observed that the dilated image responds similarly to the uncompressed image in Fig. 4. Analogously, in Fig. 8, we compare the histograms deriving from the erosion detector applied to two eroded images, one with the same structuring element and the other with a different one. Also
 255 in this case, the image filtered with a different mask responds as unfiltered. Finally, in Fig. 9 we show the case of application of the erosion detector to two images filtered with structuring elements belonging to the same group (i.e., one can be obtained from the other by dilation). As expected from Theorem 2, the
 260 two histograms are almost overlapped, since both show the statistical properties of a filtered image.

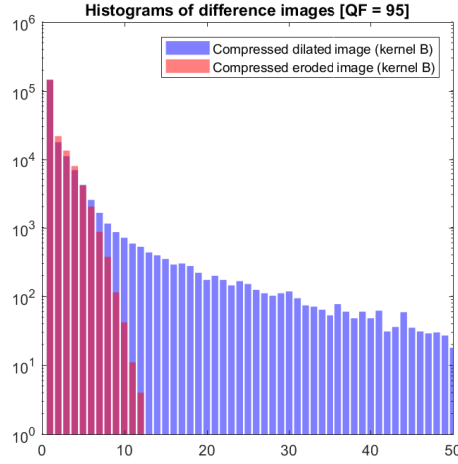


Figure 7: Histograms resulting from dilated and eroded images produced with the same structuring element, after compression at QF=95 and erosion detection.

Given the substantial equivalence of unfiltered and differently filtered images

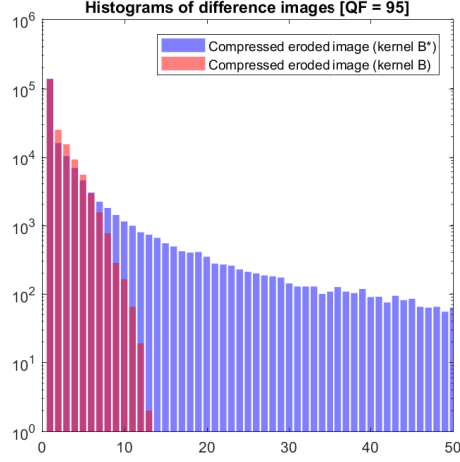


Figure 8: Histograms resulting from eroded images produced with unrelated structuring elements, after compression at QF=95 and erosion detection.

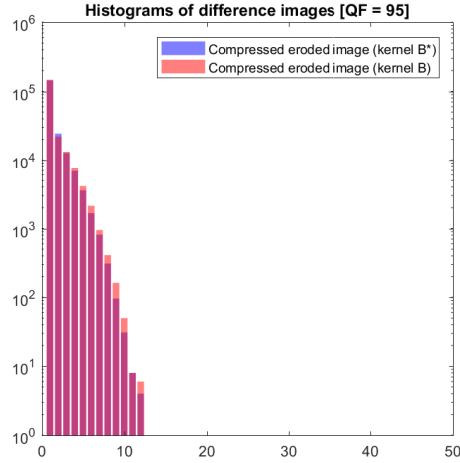


Figure 9: Histograms resulting from eroded images produced with structuring element B and its dilated version B^* , after compression at QF=95 and erosion detection.

from the point of view of the detector, and for the purpose of balancing the cardinality of the classes, we decided to limit the number of histograms to be fed into the SVM training process to 144, as follows:

- 72 (36×2) unfiltered compressed images fed to both close and open operators for every structuring element (labelled as *uncompressed*)

- 36 eroded compressed images fed to the close operator with the matching structuring element (labelled as *eroded*)
- 270 • 36 dilated compressed images fed to the open operator with the matching structuring element (labelled as *dilated*).

5. Experimental Results and Discussion

In this section, all experimental tests carried out are described. In subsection IV-A, the selected datasets and the processing of their content are presented, together with results related to uncompressed data; while subsection IV-B is 275 dedicated to the analysis of compressed data. All tests are performed using Python 3.6 and libSVM on a standard PC (Macbook Pro 2016 2,3GHz 4-kernel Intel Core i5, 8GB ram).

5.1. Experimental Results on Uncompressed Images

280 Since the detection strategy in this case is the very same proposed in [1], we followed their general approach for deriving results relative to uncompressed gray-scale images. Each image has been processed with erosion and dilation operators considering all the 36 structural elements, obtaining the following number of filtered images:

- 285 • UCID $\rightarrow 1338 \times 36 \times 2 = 96336$
- DRESDEN $\rightarrow 1189 \times 36 \times 2 = 85608$
- RAISE-1k $\rightarrow 1000 \times 36 \times 2 = 72000$

All images, along with their unprocessed versions, were fed to both dilation and erosion detectors. For each image, all 36 structural elements are tested, 290 returning either the largest kernel with perfect match between input and output or no detection if all kernels fail. All datasets result in 100% accuracy in discriminating the presence and the type of morphological filter, as reported in Table 2.

Table 2: Detection accuracy for all three datasets.

FILTER	DETECTOR	
	erosion	dilation
no filter	0%	0%
erosion	100%	0%
dilation	0%	100%

5.2. Experimental Results on Compressed Images

295 In order to test the proposed approach on JPEG compressed images, we considered a set of seven different quality factors with $QF \in \{100, 95, 90, 85, 80, 75, 70\}$, with 14 (7×2) binary classifiers, respectively, using a Gaussian kernel with grid-search for the parameters. We apply k-Fold validation with $k = 10$.

5.2.1. Classification Results - Unprocessed vs Filtered Input

300 This first test is designed to assess performance when discriminating the presence of morphological filtering in a specific compressed image. For each image belonging to the test sets, the 36 histograms extracted from unprocessed images as well as their 36 derived from eroded (dilated) contents with correct detector combinations are classified.

5.2.2. Classification Results - Unmatched Filtered Type Input

305 In this test case, the classifier of a specific type of morphological filter is fed with all the 36×36 histograms derived from each image processed with unmatched morphological operator. For example, dilated images are input to the detector dedicated to the erosion operator, and viceversa. The datasets have
310 been used in their entirety.

5.2.3. Classification Results - Structural Element Discrimination

This last test is devoted to asses accuracy in evaluating the peculiar kernel that was adopted in the input filter procedure, assuming the same morphological

Table 3: Results on all three datasets using SVM with RBF kernel, 10-fold cross validation.

Dataset	Operator	QF = 100	95	90	85	80	75	70
UCID	Erosion	100	90.86	82.62	79.63	77.45	67.41	64.42
	Dilation	100	90.16	82.86	79.95	76.80	68.77	64.94
Dresden	Erosion	100	97.56	96.94	95.20	88.73	79.85	78.34
	Dilation	100	97.93	96.82	96.11	88.74	81.08	75.08
Raise	Erosion	100	98.66	96.25	94.82	89.00	80.42	78.55
	Dilation	100	97.98	97.43	93.72	91.02	80.49	78.53

operator for both detector and filter. All kernels are applied by the corresponding detector, and the structural element resulting with the highest classification score is selected as decision output. In total, each image is tested 36×36 times, hence the same number of histogram as in the previous test case is considered. In Tables ??, ?? and ??, cumulative accuracy results for each dataset and each detector trained on the respective 80% are presented. The various kernels have been divided into three main groups, depending on their dimension and the complexity of their shape.

COMMENTS ON ALL RESULTS ARE COMPLETELY MISSING

6. Conclusions

In this work we propose an effective detection strategy to assess the use of morphological filtering in a gray-scale context. We deal with uncompressed images proposing a deterministic approach, reflection of the binary domain scenario, based on mathematical properties enjoyed by basic morphological operators. We additionally propose a modified pipeline to detect morphological processing in compressed images, exploiting difference histogram information as feature for Support Vector Machine classification. Finally, we present a testing phase in which both uncompressed and compressed scenarios are taken into

Table 4: Results on erosion detection on Table 5: Results on dilation detection on UCID using SVM with RBF kernel, 10-fold cross validation. UCID using SVM with RBF kernel, 10-fold cross validation.

K	QF = 100	95	90	85	80	75	70
1	100	90.42	83.42	79.06	75.83	64.25	63.34
2	100	90.89	82.73	79.7	76.23	65.2	64.23
3	100	90.34	82.57	80.69	77.19	66.06	64.91
4	100	89.61	83.06	80.74	76.99	65.31	63.92
5	100	90.15	83.14	80.91	77.62	65.09	62.95
6	100	90.56	82.49	81.42	78.42	65.55	63.56
7	100	91.2	82.67	81.03	78.66	66.22	64.53
8	100	92.2	82.62	80.17	78.19	65.24	65.45
9	100	92.69	83.59	80	79.1	65.9	64.87
10	100	92.89	84.08	80.65	79.67	65.78	64.5
11	100	93.09	83.41	79.88	80.26	65.59	65.28
12	100	93.48	83.63	80.87	80.08	64.86	65.41
13	100	94.47	83.62	80.73	79.93	64.35	64.61
14	100	93.59	84.32	80.25	79.59	64.49	65.6
15	100	94.4	84.02	79.3	80.32	65.07	64.72
16	100	88.41	82.22	80.45	76.24	69.13	62.8
17	100	88.49	83.18	81.17	76.4	69.07	63.66
18	100	88.78	83.72	81.99	76.76	69.08	63.69
19	100	89.09	83.29	82.21	76.7	68.8	63.53
20	100	89.07	83.67	82.96	77.01	69.23	64.52
21	100	88.87	83.86	83.18	76.62	69.86	64.71
22	100	89.13	84.17	83.86	76.12	69.63	65.69
23	100	89.99	84.82	83.4	76.52	70.3	65.67
24	100	90.35	84.95	83.55	77.34	70.59	65.73
25	100	90.19	84.52	84.19	78.11	70.92	65.93
26	100	89.87	80.42	74.24	75.44	68.14	62.58
27	100	90.83	81.14	74.92	75.64	68.08	62.74
28	100	90.44	81.34	75.37	75.18	67.81	62.5
29	100	90.33	80.88	76.1	75.88	68.61	62.69
30	100	89.98	80.55	75.74	75.71	68.24	62.64
31	100	90.61	80.2	75.41	76.34	67.99	63.05
32	100	90.67	80.56	76.02	76.72	68.44	63.03
33	100	91.31	80.39	75.64	77.12	68	63.58
34	100	91.03	80.48	76.41	77.92	68.24	63.61
35	100	91.34	80.29	77.04	77.78	68.29	64.04
36	100	92.26	80.36	77.5	78.46	69.2	64.03
Avg.	100	90.86	82.62	79.63	77.45	67.41	64.12

K	QF = 100	95	90	85	80	75	70
1	100	89.24	83.18	80.05	75.29	65.35	63.34
2	100	88.4	82.29	81.01	76.16	65.08	63.93
3	100	88.1	81.66	81.54	75.77	65.49	64.77
4	100	88.11	82.34	81.51	75.33	65.17	65.4
5	100	89.09	82.67	82.35	74.89	65.95	66.36
6	100	89.99	82.85	82.43	75.42	65.94	67.35
7	100	89.28	82.35	83.15	75.81	65.53	67.89
8	100	89.9	83.04	82.9	75.06	66.12	68.67
9	100	90.46	83.42	82.3	75.99	66.64	67.95
10	100	91.03	82.55	81.76	75	67.59	68.91
11	100	90.76	83.13	80.9	75	67.69	68.3
12	100	91.28	83.21	81.69	75.84	67.9	67.33
13	100	91.44	83.85	81.01	76.02	68.6	66.94
14	100	90.49	83.33	81.7	76.56	68.58	66.35
15	100	91.33	84.22	82.61	75.65	69.13	66.05
16	100	90.05	82.22	81.15	77.25	70.23	62.8
17	100	90.66	82.24	81.36	77.96	70.63	62.47
18	100	90.5	82.21	81.39	78.31	70.22	63.29
19	100	90.14	82.77	81.87	78.69	70.71	63.16
20	100	89.72	83.18	81.64	78.59	70.46	63.26
21	100	89.68	83.39	81.82	78.39	70.2	63.25
22	100	89.94	83.58	82.17	78.19	70.05	63.96
23	100	90.06	83.57	82.45	77.88	69.65	64.52
24	100	89.97	83.96	83.34	78.36	70.41	64.91
25	100	90.89	84.61	83.67	77.88	70.18	64.91
26	100	89.91	81	73.87	75.78	69.02	62.27
27	100	89.73	80.83	74.19	76.59	69.83	63.22
28	100	89.99	80.75	74.78	76.2	70.08	63.66
29	100	89.58	81.46	75	76.21	70.63	63.38
30	100	89.76	82.18	74.7	76.52	70.24	63.19
31	100	90.08	82.47	75.24	76.92	70.01	63.77
32	100	90.73	82.92	76.12	77.72	69.69	63.46
33	100	90.41	82.88	75.96	78.03	69.94	64.2
34	100	91.27	83.3	76.42	78.67	70.55	64.98
35	100	91.62	84.22	77.26	78.44	70.67	64.63
36	100	92.09	85.22	76.96	78.57	71.66	65.01
Avg.	100	90.16	82.86	79.95	76.80	68.77	64.94

consideration. Results show the effectiveness of our proposed approach in both cases.

References

- [1] F. G. De Natale, G. Boato, Detecting morphological filtering of binary images, IEEE Transactions on Information Forensics and Security 12 (5) (2017) 1207–1217.

Table 6: Results on erosion detection on Table 7: Results on dilation detection on Dresden using SVM with RBF kernel, 10-fold Dresden using SVM with RBF kernel, 10-fold cross validation. cross validation.

K	QF = 100	95	90	85	80	75	70
1	100	99.03	98.85	97.01	87.43	78.63	76.19
2	100	99.04	97.91	97.24	88.17	78.3	76.7
3	100	98.32	97.83	97.67	89.16	78.64	76.22
4	100	97.41	97.41	97.41	88.31	79.59	76.2
5	100	97.12	96.92	96.75	88.29	78.84	76.3
6	100	97.74	97.28	95.78	87.49	79.73	76.66
7	100	98.66	97.74	95.15	87.41	79.33	77.39
8	100	98.18	97.22	94.63	87.22	78.57	77.18
9	100	97.72	96.58	94.76	87.66	79.42	76.73
10	100	96.76	96.45	93.76	87.88	78.93	77.3
11	100	95.9	95.9	94.61	88.45	78.02	78.02
12	100	96.28	95.93	95.17	88.11	78.05	77.9
13	100	96.15	96.15	94.33	87.41	78.76	78.35
14	100	97	96.73	95.24	86.53	78.35	78.35
15	100	96.34	96.34	95.8	86.72	79.28	79.02
16	100	98.95	97.93	96.52	89.32	80.03	82.23
17	100	98.2	97.8	97.01	89.85	79.32	81.79
18	100	97.58	96.91	96.81	90.15	79.56	82.78
19	100	97.84	97.59	96.51	90.05	79.4	83.08
20	100	98.17	98.17	97.21	89.45	80.18	83.64
21	100	98.73	97.78	96.96	89.25	79.99	83.46
22	100	98.09	97.98	96.56	88.97	79.43	84.22
23	100	98.17	97.66	95.69	88.55	79.61	84.65
24	100	98.03	96.72	95.69	89	78.99	84.18
25	100	97.07	97.07	95.62	88.3	78.83	84.58
26	100	98.03	96.65	93.89	89.3	81.44	73.26
27	100	97.22	95.72	94.15	88.9	82.37	73.62
28	100	97.95	96.57	94.19	89.56	82.33	73.98
29	100	97.84	96.58	93.67	89.71	81.64	74.6
30	100	98.19	96.44	94.08	90.29	81.11	75.4
31	100	97.97	96.06	93.95	90.16	81.26	75.12
32	100	97.16	96.71	93.5	89.64	81.41	75.53
33	100	96.67	96.27	93.16	88.65	80.83	75.87
34	100	96.15	96.15	92.9	89.32	81.14	76.29
35	100	96.68	96.25	92.03	89.67	81.31	76.6
36	100	95.76	95.69	91.64	89.83	81.89	76.76
Avg.	100	97.56	96.94	95.20	88.73	79.85	78.34

K	QF = 100	95	90	85	80	75	70
1	100	98.32	98.32	96.74	87.78	79.34	73.81
2	100	97.86	97.86	96.67	88.29	79.2	74.7
3	100	98.41	98.16	97.06	89.27	79.79	74.9
4	100	97.59	97.59	96.72	88.79	80.75	73.98
5	100	96.9	96.9	96.5	88.14	80.9	73.64
6	100	97.26	97.26	96.03	88.85	80.69	74.33
7	100	96.35	96.35	96.35	88.18	79.84	74.31
8	100	95.9	95.9	95.87	88.43	79.66	74.23
9	100	96.47	96.18	96.18	87.66	80.51	74.3
10	100	97.34	97.14	96.73	87.65	79.95	73.4
11	100	96.93	96.93	96.75	87.2	80.72	72.66
12	100	97.7	96.52	96.39	87.23	81.69	72.22
13	100	97.37	96.36	95.62	87.53	81.27	72.15
14	100	98.35	95.99	95.99	86.79	80.45	72.65
15	100	97.95	95.26	95.26	87.78	79.62	72.27
16	100	98.83	97.58	96.86	90.24	80.21	75.01
17	100	99.81	98	97.47	89.36	80.72	74.82
18	100	99.26	98.06	98.06	88.43	81.13	74.74
19	100	99.05	97.06	97.06	89.2	81.46	75.02
20	100	99.96	97.5	97.21	88.78	81.36	75.73
21	100	99.53	97.17	97.17	88.51	81.68	76.2
22	100	99.12	97.52	97.52	88.51	81.56	75.7
23	100	98.32	96.7	96.7	88.83	81.32	75.99
24	100	97.5	95.83	95.83	89.82	81.12	76.95
25	100	98.05	96.75	95.38	89.64	80.21	77.03
26	100	97.84	97.51	94.81	89.69	82.31	74.12
27	100	98.45	97.07	94.71	90.24	81.63	74.83
28	100	98.65	96.95	95.65	90.14	81.76	75.04
29	100	98	96.53	96.16	89.31	81.92	75.79
30	100	97.64	97.21	95.28	90.04	82.78	75.83
31	100	97.06	96.36	95.41	89.09	82.69	76.52
32	100	97.75	95.98	95.35	89.21	82.52	77.19
33	100	97.67	95.95	95.21	88.83	82.3	77.55
34	100	98.33	95.31	94.61	88.82	81.63	77.79
35	100	97.44	96.01	94.76	89.09	82.55	78.31
36	100	96.55	95.67	93.8	89.14	81.79	79.17
Avg.	100	97.93	96.82	96.11	88.74	81.08	75.08

[2] M. Stamm, M. Wu, K. Liu, Information forensics: an overview of the first decade, IEEE Access (2013) 167–200.

[3] H. Farid, Photo forensics, 2016.

[4] A. T. Ho, Handbook of digital forensics of multimedia data and devices, John Wiley & Sons, 2015.

[5] A. Piva, An overview on image forensics, ISRN Signal Processing.

Table 8: Results on erosion detection on Table 9: Results on dilation detection on
 Raise using SVM with RBF kernel, 10-fold Raise using SVM with RBF kernel, 10-fold
 cross validation. cross validation.

K	QF = 100	95	90	85	80	75	70
1	100	98.78	97.34	94.23	88.17	78.26	77
2	100	98.97	97.53	94.54	88.53	78.57	77.63
3	100	99.03	97.16	95.24	87.96	77.6	76.94
4	100	98.65	96.34	94.41	87.19	78.56	76.42
5	100	99.08	96.15	94.82	86.43	78.8	76.53
6	100	98.16	95.42	94.05	86.89	77.9	76.45
7	100	98.17	95.96	93.78	85.98	77.18	77.18
8	100	97.99	95.47	94.61	86.4	77.76	76.68
9	100	97.97	96.4	95.26	86.05	78.21	77.42
10	100	97.96	95.68	94.33	86.19	78.35	78.25
11	100	97.27	96.43	93.35	85.98	78.16	78.16
12	100	97.42	97.29	94.21	85.16	78.02	78.02
13	100	97.82	97.46	94.98	84.73	77.67	77.67
14	100	96.87	96.87	95.76	84.48	77.95	77.95
15	100	95.97	95.97	95.97	85.26	77.11	77.11
16	100	98.55	98.04	96.94	91.52	82.99	82.22
17	100	98.8	98.03	97.65	91.63	83.14	81.96
18	100	99.74	98.96	96.69	90.8	82.75	81
19	100	98.83	98.83	96.37	90.57	83.32	81.53
20	100	98.58	98.58	96.4	90.51	82.36	81.39
21	100	98.88	97.66	97.19	90.98	81.42	81.13
22	100	98.85	96.8	96.8	90.39	80.9	80.9
23	100	99.06	97.35	96.13	90.51	80.11	80.04
24	100	99.47	96.72	95.33	90.19	80.86	79.3
25	100	99.94	96.1	95.21	90.71	79.97	78.6
26	100	99.32	95.18	95.18	91.67	80.78	78.27
27	100	99.55	95.64	94.86	92.37	81.04	79.24
28	100	99.84	94.67	94.67	91.68	81.96	80.19
29	100	99.31	94.48	94.48	91.66	82.47	79.48
30	100	99.09	93.48	93.48	91.1	83.07	78.72
31	100	99.22	93.21	93.21	90.75	83.6	77.83
32	100	99.76	93.58	92.95	90.37	83.68	77.71
33	100	98.82	94.35	92.19	90.34	83.25	76.79
34	100	98.21	94.94	92.48	90.3	82.73	77.3
35	100	98.2	94.98	93	90.04	82.23	77.45
36	100	99.12	95.93	92.68	90.56	82.54	77.42
Avg.	100	98.66	96.25	94.82	89.00	80.42	78.55

K	QF = 100	95	90	85	80	75	70
1	100	98.22	97.81	94.74	88.46	77.85	77.46
2	100	98.07	98.07	93.79	88.97	76.87	76.73
3	100	98.25	97.33	93.83	89.76	76.98	76.14
4	100	99.04	98.33	94.55	90.07	76.83	75.66
5	100	99.04	99.04	95.13	90.22	76.34	74.74
6	100	99.12	99.12	94.24	91.18	75.63	75.42
7	100	99.75	99.72	94.73	91.09	75.31	75.31
8	100	99.25	99.25	93.81	91.07	74.31	74.31
9	100	99.02	98.36	94.58	91.61	73.89	73.89
10	100	98.94	97.53	95.42	91.52	74.45	74.45
11	100	98.48	97.41	94.56	90.57	74.17	74.17
12	100	97.59	97.59	94.25	89.65	73.83	73.83
13	100	96.83	96.83	95.24	90.63	74.53	73.67
14	100	96.17	96.17	94.95	91.07	74.61	73.2
15	100	95.26	95.26	94.62	90.53	74.11	72.3
16	100	99.36	97.12	96.13	92.52	82.68	81.93
17	100	99.49	97.96	95.71	93.43	82.58	81.13
18	100	99.92	98.49	96.06	92.55	83.06	80.91
19	100	99.92	98.23	96.35	91.65	83.39	80.53
20	100	98.15	98.15	96.87	92.21	83.2	80.4
21	100	97.56	97.56	96.04	92.54	83.23	80.29
22	100	97.97	96.76	95.07	92.03	84.19	80.78
23	100	97.49	97.09	94.21	92.03	84.86	81.53
24	100	98.19	96.81	93.28	91.36	84.09	81.77
25	100	98.14	97.07	92.32	90.7	84.6	82.03
26	100	97.62	97.62	91.68	91.52	83.68	81.25
27	100	96.9	96.9	90.72	90.72	82.92	80.97
28	100	96.95	96.95	90.25	90.25	83.39	81.19
29	100	96.87	96.02	90.94	90.86	84.3	80.67
30	100	96.87	96.87	91.06	90.65	83.8	80.4
31	100	96.3	96.3	90.89	90.44	84.72	81.05
32	100	96.97	96.39	90.12	90.12	84.97	82.03
33	100	97.66	97.08	91.1	91.1	85.53	81.23
34	100	97.25	96.44	91.9	91.9	86.06	81.1
35	100	97.73	96.94	92.24	91.36	85.91	82.08
36	100	96.86	96.86	92.68	90.48	86.87	82.59
Avg.	100	97.98	97.43	93.72	91.02	80.49	78.53

- [6] H. Sencar, N. Memon (Eds.), Digital Image Forensics - There is more to a picture than meets the eye, Springer, 2013.
- [7] D. Cozzolino, L. Verdoliva, Noiseprint: a cnn-based camera model fingerprint, IEEE Transactions on Information Forensics and Security.
- [8] A. D. Rosa, A. Piva, M. Fontani, M. Iuliani, Investigating multimedia contents, in: IEEE International Carnahan Conference on Security Technology (ICCST), 2014, pp. 1–6.

Table 10: Confusion matrix on erosion detection for multiple kernels. Dataset: Raise, QF = 90, full resolution. Values are normalized and are in percentage.

	1	2	3	4	5	6	7	8	9	10	11	12	13	14	15	16	17	18	19	20	21	22	23	24	25	26	27	28	29	30	31	32	33	34	35	36	
1	0	0	0	0	0	0	0	0	0	0	0	0	0	0	0	0	0	0	0	0	0	0	0	0	0	0	0	0	0	0	3	0	0	0	0		
2	13	87	0	0	0	0	0	0	0	0	0	0	0	0	0	0	0	0	0	0	0	0	0	0	0	0	0	0	0	0	0	0	0	0	0		
3	0	0	98	0	0	0	0	0	0	0	0	0	0	0	0	0	0	0	0	0	0	0	0	0	0	0	0	0	0	0	2	0	0	0	0		
4	0	0	0	96	0	0	0	0	0	0	0	0	0	0	0	0	0	0	0	0	1	0	0	0	0	3	0	0	0	0	0	0	0	0	0		
5	1	0	0	0	99	0	0	0	0	0	0	0	0	0	0	0	0	0	0	0	0	0	0	0	0	0	0	0	0	0	0	0	0	0	0		
6	0	2	0	0	0	96	0	0	0	0	0	0	0	0	0	0	0	0	0	0	0	0	1	0	0	0	0	0	0	1	0	0	0	0	0		
7	0	0	0	0	0	0	100	0	0	0	0	0	0	0	0	0	0	0	0	0	0	0	0	0	0	0	0	0	0	0	0	0	0	0	0		
8	0	0	1	0	0	0	0	99	0	0	0	0	0	0	0	0	0	0	0	0	0	0	0	0	0	0	0	0	0	0	0	0	0	0	0		
9	0	0	0	2	0	0	1	0	95	0	0	0	0	0	0	0	0	1	0	0	0	0	0	0	1	0	0	0	0	0	0	0	0	0	0	0	
10	30	0	0	0	0	0	0	0	0	69	0	0	0	0	0	0	0	0	0	0	0	0	0	0	0	0	0	0	0	0	0	1.4	0	0	0		
11	2	0	0	1	0	0	0	0	0	0	97	0	0	0	0	0	0	0	0	0	0	0	0	0	0	0	0	0	0	0	0	0	0	0	0		
12	0	0	0	0	0	0	0	0	0	0	0	94	0	0	0	0	0	0	0	0	0	2.9	0	0	0	0	0	0	0	0	0	0	2.9	0	0		
13	0	0	0	1	0	0	0	0	0	0	0	0	93	0	0	0	0	0	0	3.8	0	0	0	0	0	0	0	0	0	0	0	0	0	0	1.9		
14	0	0	0	0	0	0	0	0	0	0	0	0	0	98	0	0	0	0	0	0	0	0	0	0	0	0	0	0	0	2	0	0	0	0	0		
15	33	33	0	0	0	0	0	0	0	0	0	0	0	0	0	33	0	0	0	0	0	0	0	1.4	0	0	0	0	0	0	0	0	0	0	0	0	
16	48	0	0	0	0	0	0	1	1	0	0	0	0	0	0	0	48	0	0	0	0	0	0	0	1	0	0	0	0	0	0	0	0	0	0	0.5	
17	0	45	5.9	0	1.8	0	0	0	0	0	0	0	0	0	0	0	0	45	0	0	0	0.9	1.8	0	0	0	0	0	0	0	0	0	0	0	0	0	
18	0	0	48	0	0	1.9	0	0	0	0	0	0	1.9	0	0	0	0	48	0	0	0	0	0	0	0	0	0	0	0	0	0	0	0	0	0	0	
19	0	0	0	48	0	0	0	1.5	0	0	0	2	0	0	0	0	0	0	48	0	0	0	0	0	0	0	0	0	0	0	0	0	0	0	0	0	
20	1	0	0	0	0	0	0	0	0	0	0	0	0	0	0	0	0	0	0	99	0	0	0	0	0	0	0	0	0	0	0	0	0	0	0		
21	12	0	0	0	0	0	2.5	0	0	2.5	0	0	0	0	0	0	0	0	0	0	0	82	0	0	0.8	0	0	0	0	0	0	0	0	0	0	0	0
22	3.3	0	0	3.3	0	0	0	0	0	4.1	0	0	0	0	3.3	3.3	0	0	0	0	0	0	79	0	0	0	0	0	0	0	0	3.3	0	0	0	0	
23	7	0	0	0	3.5	0	0	0	0	0	0	0	0	0	0	0	0	0	0	0	0	0	85	0	0	0	0	0	0	0	0.9	0	0	3.5	0	0	
24	5.8	0	0	0	0	0	0	0	6.7	0	0	0	2.5	0	0	0	4.2	0	0	0	0	0	0	81	0	0	0	0	0	0	0	0	0	0	0	0	
25	4.7	0	0	0	0	0	10	0	0	0	0	0	0	3.9	0	0	0	0	0	0	0	0	0	76	0	5.5	0	0	0	0	0	0	0	0	0		
26	1.9	0	8.6	10	36	0	0	0	0	1.5	0	0	0	0	0	0	0	0	0	0	0	0	0	0	0	36	0	0	2.6	0	0	1.1	0	0	2.6		
27	19	20	0	0	0	0	0	1.8	0	0	0	1	0	18	20	0	0	0	0	0	1.4	0	0	0	0	0	20	0	0	0	0.2	0	0	0	1	0	
28	19	19	0	0	0	0	0	0	0	0	0	0.8	0	0	19	0	19	0	0.8	0	0	0.4	0	0	0	0.8	0	0	19	1	0	0	1	0	0.6	0	
29	5.9	0	31	0	1	0	0	1.3	0	7.5	1	0	0	1	0	0	1.6	0	0	0	0	0	14	1.6	1.6	0	0	0	31	0	0	0	0	0	1.6	0	
30	7.8	1.2	0	37	0	0.8	0	0	0	1.6	0.8	0	0	0	0	0	0.8	0	2	0	0.4	0	9	0	1.2	0	0	0	37	0	0	0.4	0	0	1.2	0	
31	6.2	1.6	0	0.8	0	0	25	0	0	0	0	1.1	0	25	1.1	0	0.3	0	1.6	0	0	0.8	0	0	0	9.7	0	0.5	0	25	0	0	1.3	0	0		
32	6.7	0	3	1	0	0.6	0	19	1.6	0	0.6	0	19	0	0	3.2	0	0	0	0	0	0.4	0	0	6.7	0	0	0.8	1	8.3	0	8.5	19	0.8	0	1.2	
33	1.9	1.3	1.7	0	0	0	0.2	1.7	0	20	0	20	0	0	1.1	0	0	1.1	1.5	6.9	0	0	0.9	0	0	0.6	3.2	0	7.8	1.1	0	7.8	20	0	0	0.4	
34	2.1	0.5	0	0	0.8	0.5	0	25	0	25	0	0	0	0.8	0	0	1.6	0	1.1	0	1.3	1.3	0	0	0.8	3.4	1.1	3.2	0	4	1.6	0	0	25	0	0.8	
35	14	14	0	0	14	0	0	3.4	0	0	0	0	5.2	0	14	0	8	0	0	0	0.7	6.2	1.9	0.9	1	0.4	0	0	0	0.7	0	0.6	0.7	0.1	0	14	0
36	8.1	8.1	1	3.8	0.2	8.1	0.7	0.2	1.2	0.4	2.1	0.2	2.1	0.3	6.6	6.6	6.7	0.3	0.4	2.9	1.4	2	1.9	1.2	1.8	1.2	8.1	8.1	1	0.3	0.3	0.8	0.7	0.1	0.7	8.1	

[9] P. Bestagini, M. Tagliasacchi, S. Tubaro, Image phylogeny tree reconstruction based on region selection, in: IEEE International Conference on Acoustics, Speech and Signal Processing, 2016.

355 [10] Z. Dias, A. Rocha, S. Goldenstein, Image phylogeny by minimal spanning trees, IEEE Transactions on Information Forensics and Security 7 (2) (2012) 774–788.

[11] A. de Oliveira, et al., Multiple parenting phylogeny relationships in digital images, IEEE Transactions on Information Forensics and Security 11 (2) 360 (2016) 328–343.

[12] F. de O. Costa, et al., Image phylogeny forests reconstruction, IEEE Transactions on Information Forensics and Security 9 (10) (2014) 1533–1546.

[13] E. Ardizzone, A. Bruno, G. Mazzola, Copy-move forgery detection by matching triangles of keypoints, IEEE Transactions on Information Forensics and Security 10 (10) (2015) 2084–2094.

- [14] D. Cozzolino, G. Poggi, L. Verdoliva, Efficient dense-field copy-move forgery detection, *IEEE Transactions on Information Forensics and Security* 10 (11) (2015) 2284–2297.
- 370 [15] I. Amerini, L. Ballan, R. Caldelli, A. D. Bimbo, G. Serra, A SIFT-based forensic method for copy-move attack detection and transformation recovery, *IEEE Transactions on Information Forensics and Security* 6 (3) (2011) 1099–1110.
- [16] D. Cozzolino, G. Poggi, L. Verdoliva, Splicebuster: a new blind image splicing detector, in: *IEEE Workshop on Informations Forensics and Security (WIFS)*, 2015, pp. 1–6.
- 375 [17] X. Zhao, S. Wang, S. Li, J. Li, Passive image-splicing detection by a 2-D noncausal Markov model, *IEEE Transactions on Circuits and Systems for Video Technology* 25 (2) (2015) 185–199.
- [18] D. Vázquez-Padín, F. Pérez-González, P. Comesaña-Alfaro, A random matrix approach to the forensic analysis of upscaled images, *IEEE Transactions on Information Forensics and Security* 12 (9) (2017) 2115–2130.
- 380 [19] C. Pasquini, G. Boato, F. Pérez-González, Statistical detection of JPEG traces in digital images in uncompressed formats, *IEEE Transactions on Information Forensics and Security* 12 (12) (2017) 2890–2905.
- 385 [20] V. Conotter, H. Farid, G. Boato, Detecting photo manipulation on signs and billboards, in: *IEEE International Conference on Image Processing (ICIP)*, 2010.
- [21] E. Kee, J. O’Brien, H. Farid, Exposing photo manipulation from shading and shadows, *ACM Transactions on Graphics* 33 (165) (2014) 1–21.
- 390 [22] M. Iuliani, G. Fabbri, A. Piva, Image splicing detection based on general perspective constraints, in: *IEEE Workshop on Informations Forensics and Security (WIFS)*, 2015, pp. 1–6.

- 395 [23] K. Bahrami, A. Kot, L. Li, H. Li, Blurred image splicing localization by exposing blur type inconsistency, *IEEE Trans. on Information Forensics and Security* 10 (5) (2015) 999–1009.
- [24] G. Cao, Y. Zhao, R. Ni, X. Li, Contrast enhancement-based forensics in digital images, *IEEE Trans. on Information Forensics and Security* 9 (3) (2014) 515–525.
- 400 [25] G. Cao, Y. Zhao, R. Ni, A. Kot, Unsharp masking sharpening detection via overshoot artifacts analysis, *IEEE Signal Processing Letters* 18 (10) (2011) 603–607.
- [26] M. Kirchner, J. Fridrich, On detection of median filtering in digital images, in: *SPIE*, vol. 7541, (2010), pp. 101–112.
- 405 [27] G. Cao, Y. Zhao, R. Ni, L. Yu, H. Tian, Forensic detection of median filtering in digital images, in: *IEEE Int. Conf. on Multimedia and Expo, ICME2010*, (2010), pp. 89–94.
- [28] H.-D. Yuan, Blind forensics of median filtering in digital images, *IEEE Trans. Information Forensics and Security* 6 (4) (2011) 1335–1345.
- 410 [29] X. Kang, M. C. Stamm, A. Peng, K. J. R. Liu, Robust median filtering forensics using an autoregressive model, *IEEE Trans. Information Forensics and Security* 8 (9) (2013) 1456–1468.
- [30] C. Chen, J. Ni, J. Huang, Blind detection of median filtering in digital images: A difference domain based approach, *IEEE Trans. Image Processing* 22 (12) (2013) 4699–4710.
- 415 [31] Y. Zhang, S. Li, S. Wang, Y. Q. Shi, Revealing the traces of median filtering using high-order local ternary patterns, *IEEE Signal Processing Letters* 21 (3) (2014) 275–280.
- [32] J. Chen, X. Kang, Y. Liu, Z. J. Wang, Median filtering forensics based on convolutional neural networks, *IEEE Signal Processing Letters* 22 (11) (2015) 1849–1853.
- 420

- [33] A. Haas, G. Matheron, J. Serra, Morphologie mathématique et granulométries en place, in: Annales des mines, Vol. 11, 1967, pp. 7–3.
- [34] N. M. Al-Shereefi, Morphological filter is an active tool for edge detection in noisy image, British Journal of Science 3 (2) (2012) 148–156.
- 425 [35] P. Maragos, Morphological filtering for image enhancement and feature detection, in: The Image and Video Processing Handbook, 2004.
- [36] Y. Nakagawa, A. Rosenfeld, A note on the use of local min and max operations in digital picture processing, Tech. rep., MARYLAND UNIV COLLEGE PARK COMPUTER SCIENCE CENTER (1977).
- 430 [37] G. Schaefer, M. Stich, Ucid: An uncompressed color image database, in: Storage and Retrieval Methods and Applications for Multimedia 2004, Vol. 5307, International Society for Optics and Photonics, 2003.
- [38] T. Gloe, R. Böhme, The dresden image database for benchmarking digital image forensics, Journal of Digital Forensic Practice 3 (2-4) (2010) 150–159.
- 435 [39] D.-T. Dang-Nguyen, C. Pasquini, V. Conotter, G. Boato, Raise: a raw images dataset for digital image forensics, in: ACM Multimedia Systems Conference, 2015.

Table 11: Results on erosion detection under different resolutions. Dataset: Raise, QF = 90, SVM with RBF kernel, 10-fold cross validation.

K		3000	2000	1000	500	300
	Full	x	x	x	x	x
		3000	2000	1000	500	300
1	97.34	96.45	95.24	90.32	75.25	64.75
2	97.53	95.61	95.56	89.67	74.76	64.67
3	97.16	95.62	95.62	90.38	74.85	65.53
4	96.34	94.76	94.76	90.24	74.68	64.65
5	96.15	93.93	93.93	91.18	73.91	65.15
6	95.42	94.52	93.81	92.13	73.01	64.8
7	95.96	94.73	93.33	92.99	73.45	63.99
8	95.47	94.81	92.55	92.03	73.69	64.28
9	96.4	94.46	93.54	92.63	73.3	63.63
10	95.68	95.07	94.12	92.09	74.12	63.38
11	96.43	95.84	94.85	91.36	74.01	63.62
12	97.29	94.97	94.97	91.45	73.71	62.7
13	97.46	94.51	94.3	91.2	73.04	61.96
14	96.87	95.47	95.23	91.68	73.42	62.09
15	95.97	95.97	95.97	91.42	72.81	62.62
16	98.04	98.21	98.09	92.06	85.17	67.07
17	98.03	98.03	97.9	92.18	86	66.75
18	98.96	97.23	97.23	92.4	86.25	65.98
19	98.83	98.05	96.29	93.09	86.64	66.3
20	98.58	98.22	96.41	92.47	86.42	65.64
21	97.66	97.66	96.63	93.29	86.1	66.57
22	96.8	96.8	95.76	92.56	86.91	65.59
23	97.35	96.58	96.38	92.72	87.62	66.56
24	96.72	96.72	96.52	93.48	87.72	66.71
25	96.1	96.1	96.1	92.6	86.99	65.79
26	95.18	97.46	97.46	93.03	85.16	67.32
27	95.64	95.64	95.64	92.6	84.23	67.59
28	94.67	94.67	94.67	93.12	84.65	67.38
29	94.48	94.43	94.43	93.03	84.75	66.82
30	93.48	93.48	93.48	92.47	84.83	67.3
31	93.21	93.21	93.21	91.62	85.27	67.66
32	93.58	92.96	92.5	91.35	84.94	68.55

Table 12: Results on dilation detection under different attacks. Dataset: Raise, full resolution, QF = 100, using SVM with RBF kernel, 10-fold cross validation.

K	Pepper & Salt	Gaussian (3x3)	Median Filter (3x3)	Scale (1.1x)	Scale (0.9x)
1	96.24	84.93	95.48	63.68	68.68
2	96.96	83.99	95.81	64.41	68.23
3	97.19	83.92	94.83	65.33	67.96
4	97.86	84.38	94.77	65.39	67.75
5	98.02	84.42	95.64	66	67.02
6	98.07	85.07	96.58	65.85	67.16
7	98.21	85.5	97.34	66.22	67.88
8	97.28	84.79	97.35	66.2	67.85
9	97.06	85.61	97.9	67.09	67.68
10	97.86	86.54	97.19	67.29	68.06
11	97.89	87.19	97.89	67.95	68.66
12	98.77	87.25	97.36	68.78	69.27
13	99.76	86.37	97.8	67.84	69.83
14	100	86.86	97.79	68.07	68.97
15	99.11	74.96	72.17	68.23	68.23
16	99.72	74.45	72.65	68.42	69.23
17	100	75.27	73.45	68.63	69.79
18	99.92	75.6	73.43	67.7	69.29
19	100	75.3	72.44	67.32	70.04
20	100	74.64	72.88	68.31	70.76
21	100	75.63	73.09	69.22	70
22	100	74.9	72.81	68.72	69.13
23	100	75.61	72.83	69.42	68.81
24	100	75.98	72.4	69.24	67.94
25	99.64	76.83	72.3	69.87	68.4
26	95.47	81.97	93.57	66.64	64.64
27	96.24	82.14	94.46	66.47	65.15
28	96.21	81.27	93.56	66.49	64.93
29	95.78	81.88	92.99	66.62	65.09
30	96.06	81.12	92.34	66.63	65.86
31	95.36	81.11	91.94	66.93	65.61
32	96.1	80.41	91.23	67.92	66.05
33	95.59	81.34	91.25	68.7	66.33

Table 13: Results on erosion detection on Raise under different attacks, using SVM with RBF kernel, 10-fold cross validation.

QF	Pepper & Salt	Gaussian (3x3)	Median Filter (3x3)
100	97.92	81.21	87.94
95	95.72	81.14	86.44
90	95.19	81.01	84.27
85	91.79	79.16	80.67
80	86.99	78.76	80.57
75	83.04	75.06	76.42
70	81.23	70.24	71.49

Table 14: False Positive on 200 images from RAISE on erosion Detection. Images are in raw format, full resolution. The classifiers were trained on 800 images (eroded vs. non-filtered) and tested on the rest 200 images (filtered with pepper & salt, Gaussian and median).

K	Pepper & Salt	Gaussian (3x3)	Gaussian (5x5)	Median Filter (3x3)	Median F
1	7	3	7	15	1
2	14	6	1	20	1
3	18	0	6	15	1
4	15	6	3	17	1
5	12	7	0	17	1
6	10	7	0	13	2
7	6	0	6	17	1
8	7	1	7	18	2
9	7	6	1	13	2
10	9	4	3	12	1
11	19	11	15	47	2
12	8	24	11	41	3
13	20	13	22	46	3
14	19	19	13	49	2
15	9	17	10	69	2
16	6	11	5	24	2
17	7	9	11	23	1
18	7	19	19	32	1
19	3	20	11	28	1
20	3	9	19	22	1
21	2	9	5	37	1
22	5	12	18	21	1
23	1	19	5	18	2
24	4	8	18	29	1
25	3	18	14	25	2
26	3	6	11	27	4
27	3	16	19	37	2
28	6	17	20	16	3
29	5	7	8	19	4
30	6	19	6	23	4
31	2	13	10	37	3
32	0	19	10	31	4
33	0	20	15	35	3